3-D Short-Range Imaging with Irregular MIMO Arrays Using NUFFT-Based Range Migration Algorithm

Wang, Jianping; Aubry, Pascal; Yarovoy, Alexander

Important note
To cite this publication, please use the final published version (if applicable).
Please check the document version above.

3-D Short-Range Imaging With Irregular MIMO Arrays Using NUFFT-Based Range Migration Algorithm

Jianping Wang[ID], Pascal Aubry[ID], and Alexander Yarovoy, *Fellow, IEEE*

Abstract— 3-D imaging with irregular planar multiple-input-multiple-output (MIMO) arrays is discussed. Due to signal acquisition on irregular spatial sampling grids by using these antenna arrays, the fast Fourier transform (FFT)-based imaging algorithms cannot readily be used for image formation. To avoid the application of computationally intensive coherent summation algorithms such as filtered backprojection or Kirchhoff migration, we propose a nonuniform FFT (NUFFT)-based MIMO Range Migration Algorithm (i.e., NUFFT-based MIMO-RMA) for efficient microwave imaging. The algorithm exploits NUFFT to reconstruct the wavenumber–domain spectra related to each Fourier frequency. It is generic and applicable to 3-D imaging with irregular planar MIMO arrays. The effects of irregular spatial sampling and signal bandwidth on the imaging performance and computational efficiency of the proposed algorithm are analyzed. Finally, some numerical simulations and experimental results are presented to demonstrate the performance of the proposed imaging algorithm.

Index Terms— 3-D imaging, microwave imaging, multiple-input-multiple-output (MIMO) array, nonuniform fast Fourier transform (NUFFT), range migration.

I. INTRODUCTION

ARRAY-BASED microwave imaging has been widely used for applications such as concealed weapon detection [1], ground-penetrating radar (GPR) [2], and through-the-wall imaging [3]. For these applications, various microwave imaging systems and image formation algorithms have been developed.

To obtain high cross-range resolution(s), large aperture antenna arrays are generally used for signal acquisition in these imaging systems, which are usually implemented through: phased array, synthetic aperture radar (SAR), or multiple-input-multiple-output (MIMO) array techniques. Phased arrays typically use numerous antennas to form a large aperture having a narrow beamwidth in the cross-range direction(s). However, phased arrays are usually not an economical option

for civilian applications. By contrast, the SAR and MIMO array techniques form a large effective (i.e., virtual) aperture array by moving a small antenna or array and exploiting spatial diversity of transmit and receive antenna arrays, respectively. Both techniques substantially reduce the number of antennas required for imaging array system construction, thus providing a cost-effective solution for various short-range imaging applications.

Many different short-range imaging systems have been developed using SAR, MIMO arrays, or their combinations. To obtain 3-D imaging capability, 2-D antenna arrays are needed. By exploiting the SAR technique, a 2-D array can be synthesized by moving a linear array in space. Typically, the linear array is translated with three different scanning strategies: 1) linear scanning configuration, where the linear array is moved along its broadside direction to synthesize a planar aperture; 2) cylindrical scanning configuration, where the linear array is rotated around an axis that is parallel to the array axis to form an effective array aperture over a cylindrical surface; and 3) radial-scanned SAR (Rad-SAR) configuration [4], where a linear array is rotated around its center on a plane to form a circular planar array. The linear scanning configuration has been used for fast subsurface surveys with GPR array systems while the cylindrical scanning strategy is employed for security screening of the human body [5]. As a new scanning configuration, the Rad-SAR has also been studied, for instance, to develop a forward prediction system potentially used for a tunnel boring machine [6], [7]. However, the cross-range resolution along the linear array direction is still completely determined by the dimension of the linear array aperture for a fixed operating frequency bandwidth. Therefore, a large linear array is still needed to get high cross-range resolution along the linear array direction.

To further improve the cross-range resolution and also to reduce the number of antennas needed, an MIMO-SAR array system is proposed by replacing the linear array with a 1-D MIMO array, which has been demonstrated for concealed weapon detection in both microwave and millimeter-wave frequencies [8]–[11]. It synthesizes a large effective aperture by using MIMO and SAR techniques in two cross-range directions, respectively. The collected data are conventionally focused by using filtered backprojection or Kirchhoff migration. In [11], a hybrid, i.e., Fourier-summation-based migration is developed to accelerate the image formation when the 1-D MIMO array consists of uniformly distributed

transmitters/receivers. Since the MIMO-SAR is implemented by mechanically translating or rotating a linear MIMO array along the direction perpendicular to the array axis, it usually takes a longer time for signal acquisition, which may limit its application for real-time or near real-time imaging.

Another kind of microwave imaging system is proposed and developed for real-time imaging by exploiting 2-D MIMO arrays which provide the potential for signal acquisition with one snapshot by using orthogonal waveforms/time multiplexing in different transmit channels [12]–[16]. By taking advantage of the spatial diversities of 2-D transmit and receive antenna arrays, a 2-D MIMO array can form a large effective aperture using a much smaller number of antennas, which significantly reduces the system cost without degrading image quality. For example, a quick personnel screening (QPS) system [15] was developed based on the 2-D MIMO array technique for short-range personnel screening at airports and public buildings. In [14], the optimal design of 2-D MIMO arrays for short-range imaging was discussed. In both cases, images are reconstructed using the backprojection algorithm and modified Kirchhoff migration algorithm (KMA). Although these two algorithms can produce relatively accurate images and are adaptive to arbitrary measurement configurations, their computational costs are extremely high, which makes (near) real-time imaging impractical. To address this problem, a range migration algorithm (i.e., MIMO-RMA) was developed for 3-D imaging with 2-D MIMO arrays [17]. Taking advantage of the fast Fourier transform (FFT), this MIMO-RMA algorithm significantly improves the efficiency of image formation. To further improve the efficiency, a transverse spectrum deconvolution technique [18] was proposed to implement the 5-D to 3-D mapping of the MIMO-RMA in the f-k domain. However, both algorithms are only applicable to the signals acquired with 2-D uniform rectilinear MIMO arrays. On the other hand, inversion-based algorithms are adaptive to various MIMO array imaging systems, which generally involve an optimization problem [19]. Although some iterative computational approaches exist to tackle such optimization problems, they are usually very computationally intensive. Therefore, for 3-D imaging with generic 2-D MIMO arrays, an efficient image formation algorithm, to our best knowledge, has not been described in the open literature.

In this article, we address the 3-D imaging problem with generic 2-D planar MIMO arrays and propose a nonuniform FFT(NUFFT)-based RMA (abbreviated as NUFFT-based MIMO-RMA) for efficient image formation. For microwave imaging, NUFFT [20], [21] has been used to replace the 1-D Stolt interpolation of the RMA in [22]–[25], 1-D matched filter with unequal spaced samples [26], and 3-D imaging with the Rad-SAR [4], respectively. By contrast, the proposed approach utilizes the NUFFT algorithm to estimate the signal spectra over a rectilinear grid in the frequency-wavenumber (i.e., f-k) domain from the spatial signals measured by a 2-D MIMO array, which facilitates the application of the FFT algorithm in the following steps. To account for an impact of the nonuniform distribution of spatial samples on the f-k domain spectrum computation, Voronoi decomposition is introduced to partition the transmit and receive array apertures. Similar
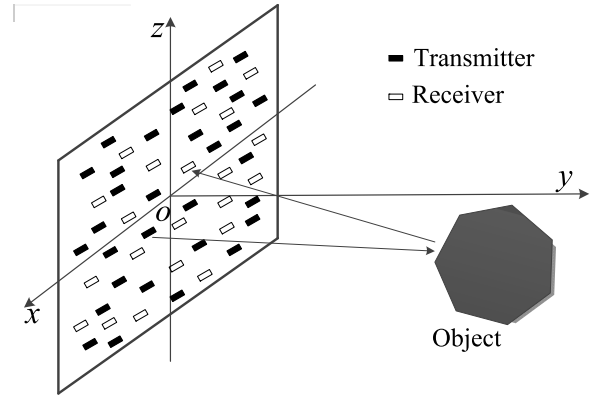

Fig. 1.   Geometrical configuration with generic planar MIMO array.

applications of Voronoi decomposition can also be found in antenna array design [27] and data gridding [28]. Moreover, to further improve the efficiency of the proposed algorithm, 1-D NUFFT is used to replace the interpolation for wavefront curvature correction [22]–[24]. Due to the use of NUFFT, the proposed algorithm, compared to the traditional MIMO-RMA, not only maintains the high computational efficiency but also is applicable for generic 2-D planar MIMO array configurations. Its imaging performance will be demonstrated through both numerical simulations and experimental measurement.

The rest of the article is organized as follows. In Section II, 3-D imaging with a generic 2-D planar MIMO array is formulated and the NUFFT-based MIMO-RMA is presented. The detailed implementation of the proposed algorithm is described in Section III. Sections IV and V demonstrate the imaging performance of the proposed algorithm through numerical simulations and experimental results, respectively. A brief comparison of the proposed algorithm and the existing ones are given in Section VI. Finally, conclusions are drawn in Section VII.

II. FORMULATION FOR 3-D IMAGING WITH A 2-D MIMO ARRAY

Here, we consider 3-D imaging with a generic 2-D planar MIMO array. A 2-D planar MIMO array is placed on the xz plane, and the y-axis points toward the illuminated scene and forms a right-handed coordinate system with the x- and z-axes. Objects are located in the near field of the MIMO array. The geometrical configuration is shown in Fig. 1.

It is assumed that the Born approximation is valid for the object scattering process. Meanwhile, a scalar formalism is considered and the antennas are assumed to be isotropic. For a transmitter and receiver pair located, respectively, at $(x_t, z_t, 0)$ and $(x_r, z_r, 0)$, the scattered signal acquired by the receiver can be represented as

$$s(t, x_t, z_t, x_r, z_r)$$
$$= \iiint_V \frac{f(x, y, z)}{16\pi^2 R_t R_r} \cdot p\left(t - \frac{R_t}{c} - \frac{R_r}{c}\right) dx\, dy\, dz \quad (1)$$

where $f(x, y, z)$ denotes the scattering coefficient of a scatterer located at (x, y, z), V is the volume occupied by the

illuminated targets, c is the speed of the electromagnetic (EM) wave, and $p(t)$ is the signal radiated by the transmitter. R_t and R_r represent the distances from the transmitter to the scatterer and from the scatterer to the receiver, which are given by

$$R_t = \sqrt{(x - x_t)^2 + y^2 + (z - z_t)^2} \tag{2}$$
$$R_r = \sqrt{(x - x_r)^2 + y^2 + (z - z_r)^2}. \tag{3}$$

Taking the Fourier transform (FT) of (1) with respect to the time t, the frequency spectrum is obtained as

$$s(f, x_t, z_t, x_r, z_r)$$
$$= P(f) \iiint_V f(x, y, z) \frac{e^{-jk(R_t + R_r)}}{16\pi^2 R_t R_r} \, dx \, dy \, dz \tag{4}$$

where $k = 2\pi f/c$ is the wavenumber related to the frequency f, and $P(f)$ is the Fourier spectrum of $p(t)$.

Using the Weyl identity for spherical waves [29], [30], the scattered signal can be represented in the frequency-wavenumber (i.e., f-k) domain as

$$s(f, x_t, z_t, x_r, z_r)$$
$$= P(f) \iiint_V f(x, y, z) \, dx \, dy \, dz$$
$$\cdot \iint \frac{-je^{-j(k_{x_t}x + k_{y_t}y + k_{z_t}z)}}{8\pi^2 k_{y_t}} e^{j(k_{x_t}x_t + k_{z_t}z_t)} \, dk_{x_t} \, dk_{z_t}$$
$$\cdot \iint \frac{-je^{-j(k_{x_r}x + k_{y_r}y + k_{z_r}z)}}{8\pi^2 k_{y_r}} e^{j(k_{x_r}x_r + k_{z_r}z_r)} \, dk_{x_r} \, dk_{z_r} \tag{5}$$

where k_{x_t}, k_{z_t}, k_{x_r}, and k_{z_r} are the Fourier counterparts of x_t, z_t, x_r, and z_r in the wavenumber domain. k_{y_t} and k_{y_r} are expressed as

$$k_{y_t} = \sqrt{k^2 - k_{x_t}^2 - k_{z_t}^2} \tag{6}$$
$$k_{y_r} = \sqrt{k^2 - k_{x_r}^2 - k_{z_r}^2}. \tag{7}$$

According to (5), the frequency–wavenumber domain spectrum of $s(f, x_t, z_t, x_r, z_r)$ can be obtained as

$$S(f, k_{x_t}, k_{z_t}, k_{x_r}, k_{z_r}) = -\frac{P(f)}{4k_{y_t}k_{y_r}} \iiint_V f(x, y, z)$$
$$\cdot e^{-j(k_x x + k_y y + k_z z)} \, dx \, dy \, dz \tag{8}$$

where

$$\begin{cases} k_x = k_{x_t} + k_{x_r} \\ k_y = k_{y_t} + k_{y_r} \\ k_z = k_{z_t} + k_{z_r}. \end{cases} \tag{9}$$

From (8), one can see that $S(f, k_{x_t}, k_{z_t}, k_{x_r},$ and $k_{z_r})$ is a FT of the object's scattering coefficient with the dispersion relations in (9). Therefore, the object's image can be reconstructed via an inverse FT

$$f(x, y, z) = \frac{1}{2\pi^3} \iiint \frac{k_{y_t}k_{y_r}}{P(f)} S(f, k_{x_t}, k_{z_t}, k_{x_r}, k_{z_r})$$
$$\cdot e^{j(k_x x + k_y y + k_z z)} \, dk_x \, dk_y \, dk_z. \tag{10}$$

Equation (10) gives an analytical approach for generic planar MIMO array imaging. Note a similar equation was derived based on the principle of stationary phase for rectilinear

MIMO array imaging in [17] and [18]. To efficiently implement the operation in (10), the spectrum $S(f, k_{x_t}, k_{z_t}, k_{x_r}, k_{z_r})$ should be first computed over a 5-D uniform rectilinear grid. Then a data mapping from 5-D [i.e., $(f, k_{x_t}, k_{z_t}, k_{x_r}, k_{z_r})$] grid to 3-D [i.e., (k_x, k_y, k_z)] grid is needed to facilitate the application of the inverse FFT(IFFT) for image formation.

To obtain the 5-D signal spectrum $S(f, k_{x_t}, k_{z_t}, k_{x_r}, k_{z_r})$ from the radar measurements $s(t, x_t, z_t, x_r, z_r)$, a 1-D FT with respect to t and two 2-D spatial FTs over the transmit and receive antenna arrays, respectively, are required. The 1-D FT can be implemented by using the FFT. However, for general planar MIMO arrays, antenna elements are irregularly distributed within the aperture, thus making 2-D FFT over transmit and receive arrays no longer applicable. Although in discrete form the signal spectrum can be obtained point by point through a Riemann sum, it is extremely time-consuming. To circumvent this problem, we suggest taking advantage of the NUFFT to accelerate the computation as discussed in the following steps.

A. Signal Spectrum Reconstruction

The signal spectrum $S(f, k_{x_t}, k_{z_t}, k_{x_r}, k_{z_r})$ can be analytically acquired by taking two 2-D FTs over both transmit and receive antenna arrays, which is expressed as

$$S(f, k_{x_t}, k_{z_t}, k_{x_r}, k_{z_r})$$
$$= \iint_{(x_t, z_t)} \iint_{(x_r, z_r)} s(f, x_t, z_t, x_r, z_r) e^{-j(k_{x_t}x_t + k_{z_t}z_t)}$$
$$\cdot e^{-j(k_{x_r}x_r + k_{z_r}z_r)} \, dx_t \, dz_t \, dx_r \, dz_r. \tag{11}$$

For general planar MIMO arrays, the antenna elements within the transmit and receive arrays take spatial samples irregularly. The spectrum in the f-k domain can be obtained by replacing the integral in (11) with the Riemann sum over the antenna elements in transmit and receive arrays

$$S(f, k_{x_t}, k_{z_t}, k_{x_r}, k_{z_r})$$
$$= \sum_{m=0}^{N_t-1} \sum_{n=0}^{N_r-1} s(f, x_{t_m}, z_{t_m}, x_{r_n}, z_{r_n}) \cdot e^{-j(k_{x_r}x_{r_n} + k_{z_r}z_{r_n})}$$
$$\cdot e^{-j(k_{x_t}x_{t_m} + k_{z_t}z_{t_m})} \Delta S_{r_n} \Delta S_{t_m} \tag{12}$$

where (x_{t_m}, z_{t_m}) denotes the position of the mth transmit antenna and (x_{r_n}, z_{r_n}) is the position of the nth receive antenna element on the plane $z = 0$. ΔS_{t_m} and ΔS_{r_n} are the areas around the sampling positions (x_{t_m}, z_{t_m}), and (x_{r_n}, z_{r_n}) over transmit and receive array apertures, respectively, which represents a spatial weighting factor for each sample. These areas can be obtained by applying the Voronoi partition to the transmit and receive apertures with the area of each Voronoi cell assigned to the corresponding sample inside that cell [27], [28]. One can see that (12) is actually a 4-D nonuniform discrete FT(NDFT), which can be rearranged as two 2-D

NDFTs

$$S(f, k_{x_t}, k_{z_t}, k_{x_r}, k_{z_r}) = \sum_{m=0}^{N_t-1} e^{-j(k_{x_t}x_{t_m}+k_{z_t}z_{t_m})} \Delta S_{t_m}$$
$$\cdot \left[\sum_{n=0}^{N_r-1} s(f, x_{t_m}, z_{t_m}, x_{r_n}, z_{r_n}) \Delta S_{r_n} \right.$$
$$\left. \cdot e^{-j(k_{x_r}x_{r_n}+k_{z_r}z_{r_n})} \right]. \quad (13)$$

According to (13), the f-k domain spectrum over a uniform regular grid can be efficiently computed by using 2-D NUFFT over transmit and receive apertures separately.

Repeating the aforementioned operations on $s(f, x_t, z_t, x_r, z_r)$ over all the discrete frequencies, the 5-D signal spectrum volume is reconstructed in the f-k domain.

B. k-Space Interpolation

As in the RMA algorithm for 3-D imaging with planar rectilinear MIMO arrays [17], a data mapping from $(f, k_{x_t}, k_{z_t}, k_{x_r}, k_{z_r})$ grid to (k_x, k_y, k_z) grid, according to the dispersion relations in (9), is needed before taking a 3-D IFFT for image reconstruction in (10). As the reconstructed signal spectrum $S(f, k_{x_t}, k_{z_t}, k_{x_r}, k_{z_r})$ is uniformly sampled over a rectilinear grid of $f, k_{x_t}, k_{z_t}, k_{x_r}$, and k_{z_r}, then the grid after mapping is uniform along the k_x and k_z directions but nonuniform along the k_y direction. To facilitate the utility of 3-D IFFT, the Stolt interpolation is typically used to obtain data over a uniform grid of (k_x, k_y, k_z), but it is very computationally intensive to obtain the expected data one by one [31]. Although the Stolt interpolation can be approximated by regular interpolation approaches such as linear, cubic, and spline interpolation to improve the efficiency, in some cases the interpolation accuracy is not sufficient. To achieve sufficient accuracy as well as high efficiency, 1-D NUFFT can be employed to replace the Stolt interpolation and a 1-D IFFT [22]–[24], which is also integrated into the proposed algorithm.

III. ALGORITHM IMPLEMENTATION

In this section, some practical aspects for the implementation of the proposed NUFFT-based MIMO-RMA are described as follows.

1) For pulse systems, the received signals are first converted to the frequency domain by applying an FFT. For step-frequency systems, this operation is not necessary. Then, signal spectra in the f-k domain should be reconstructed, which is a key step of the proposed algorithm. Considering irregular planar MIMO arrays, the signal spectra are first weighted by the areas of the discrete cells (i.e., Voronoi cells) around the related spatial sampling positions and then two 2-D NUFFTs are carried out over the transmit and receive arrays to obtain signal spectra over a regular sampling grid in the f-k domain. To avoid spatial aliasing in the focused images, the regular sampling grid in the wavenumber domain should be defined based on the Nyquist criterion.

Assuming the cross-range dimensions (i.e., along the x- and z-axes) of the field of view (FOV) are $a \times b$, the sampling intervals in the wavenumber domain should fulfill the constraints

$$\begin{cases} \Delta k_{x_t} \leq 2\pi/a, & \Delta k_{z_t} \leq 2\pi/b \\ \Delta k_{x_r} \leq 2\pi/a, & \Delta k_{z_r} \leq 2\pi/b \end{cases} \quad (14)$$

where Δk_{x_t} and Δk_{z_t} are the sampling intervals along the k_x and k_z directions of the signal spectra related to the transmit array while Δk_{x_r} and Δk_{z_r} are the corresponding k-space sampling intervals related to the receive array. To facilitate the data mapping (from 5-D to 3-D) of the signal spectra over the transmit and receive arrays, we set the sampling intervals along the corresponding dimensions equal, i.e., $\Delta k_{x_t} = \Delta k_{x_r}$, and $\Delta k_{z_t} = \Delta k_{z_r}$. After defining the sampling intervals, the number of samples along the $k_{x_t}, k_{z_t}, k_{x_r}$, and k_{z_r} dimensions are determined by the maximum wavenumber that is typically related to the maximum frequency $f_{\max}$ of the signal, which are expressed as

$$\begin{cases} N_{kx}^t = \dfrac{2\pi f_{\max}}{c \cdot \Delta k_{x_t}}, & N_{kz}^t = \dfrac{2\pi f_{\max}}{c \cdot \Delta k_{z_t}} \\ N_{kx}^r = \dfrac{2\pi f_{\max}}{c \cdot \Delta k_{x_r}}, & N_{kz}^r = \dfrac{2\pi f_{\max}}{c \cdot \Delta k_{z_r}} \end{cases} \quad (15)$$

where N_{kx}^t and N_{kz}^t denote the number of samples of the signal spectra along the k_{x_t} and k_{z_t} dimensions while N_{kx}^r and N_{kz}^r are the corresponding number of the samples along the k_{x_r} and k_{z_r} dimensions.

By performing two 2-D NUFFTs over the transmit and receive arrays, a 5-D data matrix is obtained for the signal spectra in the f-k domain. In this article, the fast Gaussian gridding-based NUFFT was used [21]. For M frequency samples, the size of the data matrix is $N_{kx}^t \times N_{kz}^t \times N_{kx}^r \times N_{kz}^r \times M$. As the wavenumbers and the frequencies relate by (6) and (7), respectively, for the transmit and receive arrays, for a particular frequency $f < f_{\max}$ the region of support (ROS) of the signal spectra in the wavenumber domain is smaller than that for the frequency $f_{\max}$. Thus, to improve the computational efficiency of signal spectrum reconstruction, one can only compute by 2-D NUFFT the samples in the wavenumber domain whose numbers are given by

$$\begin{cases} N_{kx,f}^t = \dfrac{2\pi f}{c \cdot \Delta k_{x_t}}, & N_{kz,f}^t = \dfrac{2\pi f}{c \cdot \Delta k_{z_t}} \\ N_{kx,f}^r = \dfrac{2\pi f}{c \cdot \Delta k_{x_r}}, & N_{kz,f}^r = \dfrac{2\pi f}{c \cdot \Delta k_{z_r}}. \end{cases} \quad (16)$$

These computed samples of signal spectra are located in the central area around zeros in the k_{x_t}-k_{z_t} and k_{x_r}-k_{z_r} planes, while the remaining samples are filled with zeros. Moreover, as the reconstruction of the wavenumber-domain signal spectra should be separately performed with respect to each frequency f, they can be implemented by parallel computing for further acceleration.

2) Next, the reconstructed signal spectra are multiplied by $(k_{y_t} k_{y_r}/2\pi^3 P(f))$, which removes the weighting
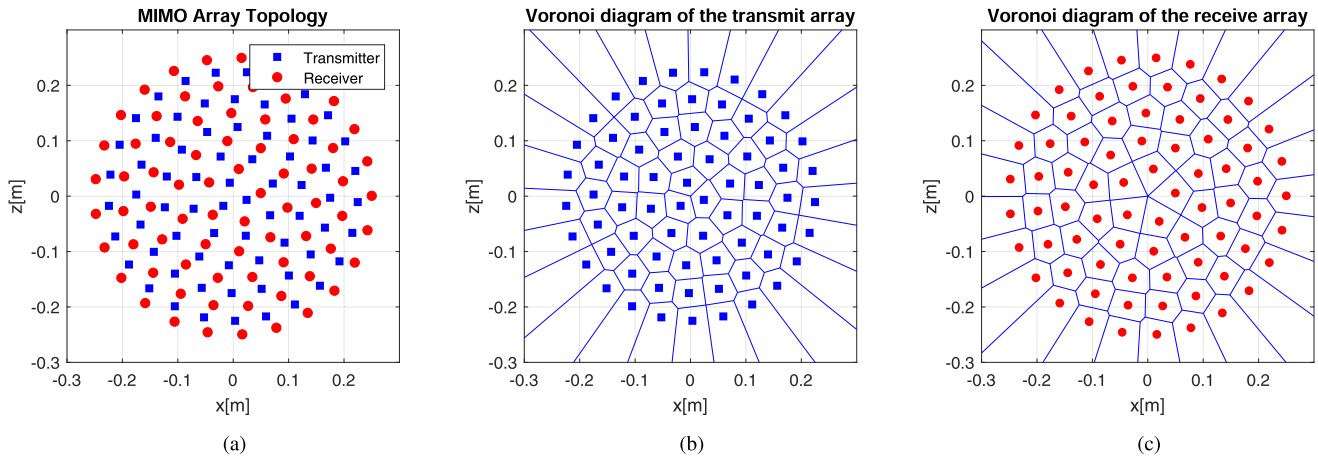
Fig. 2. MIMO array with dense samples used for numerical simulation. (a) Shows the MIMO array topology with 70 transmitters and 75 receivers. (b) and (c) Show the Voronoi diagrams associated with the transmitting and receiving arrays, respectively.

effects of the radiated waveform on the reconstructed image and also performs high-pass filtering in the f-k domain. For noisy data, this filtering process can, in principle, be replaced by more advanced filtering approaches (e.g., Wiener filter) designed based on, for instance, the minimum mean-square error (MMSE) criterion. Then, advanced filters should be designed for the signals over $[2\pi f_{\min}/c, 2\pi f_{\max}/c]$ at each quartet $(k_{x_t}, k_{z_t}, k_{x_r}, k_{z_r})$. Such an advanced filtering approach may improve the estimation of signals in the MMSE sense but at the expense of significantly increased computational load. So considering both imaging performance and computational complexity, we prefer to keep using the filtering process $(k_{y_t} k_{y_r}/2\pi^3 P(f))$ in this article. After that, a data mapping from $(f, k_{x_t}, k_{z_t}, k_{x_r}, k_{z_r})$ grid to (k_x, k_y, k_z) grid is carried out to compensate the wavefront curvature in the wavenumber domain and fuse all the information resulting from the spatial diversity of transmitters and receivers, which is a unique step of MIMO-RMA with 2-D MIMO arrays in contrast to conventional RMA with planar arrays [31]. To implement the 5-D to 3-D data mapping, interpolation is needed which can be accomplished through linear, cubic, spline, or other regular interpolation methods. For simplicity, linear interpolation is used in this article. Finally, a 3-D IFFT is taken to get a focused image of targets. To further improve the efficiency, the wavenumber-domain interpolation and the 1-D IFFT along the k_y dimension can be replaced by a 1-D NUFFT followed by a 2-D IFFT to finish the image formation. Accordingly, we distinguish the proposed imaging algorithm with these two different implementations of the data mapping as "NUFFT-based MIMO-RMA" and "NUFFT-Interp-based MIMO-RMA", respectively.

IV. NUMERICAL SIMULATIONS

The imaging performance of the proposed NUFFT-based MIMO-RMA is demonstrated by means of numerical simulations. In the first example, an irregular dense MIMO antenna
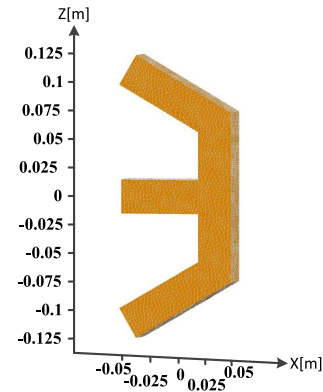

Fig. 3. Illustration of the "E"-shaped object used for the simulation.

array is used for 3-D imaging. Similar to the geometrical configuration shown in Fig. 1, the irregular MIMO array is placed on the xz plane for transmission and reception, and the y-axis points toward the scene of illumination. The MIMO array contains 145 antennas: 70 for transmission and 75 for reception (MIMO array I in Table I). The transmit antennas are placed over five circles with the radius ranging from 2.5 to 22.5 cm with steps of 5 cm, and the receive antennas are set on another five interleaved circles whose radii increase uniformly from 5 cm with steps of 5 cm. The resultant MIMO array topology is shown in Fig. 2(a). An "E"-shaped perfect electric conductor (PEC) object is placed parallel to the antenna array at a distance of 0.5 m. Fig. 3 illustrates the "E"-shaped object that is composed of four rectangular cuboids. The cuboid parallel to the z-axis is 15 cm in length while the other three have a length of 10 cm. The width and thickness of all the cuboids are 3 cm. For the MIMO array, Hertz dipoles are used as radiators. The scattered EM signals are synthesized by using the commercial EM software FEKO with the Method of Moments (MoMs) solver, which is implemented in the frequency domain. The operating frequencies are from 9 to 12 GHz with steps of 100 MHz.

Using the proposed NUFFT-based MIMO RMA, the synthetic EM data can be focused. To consider the effect of the nonuniform spatial sampling, the acquired data are
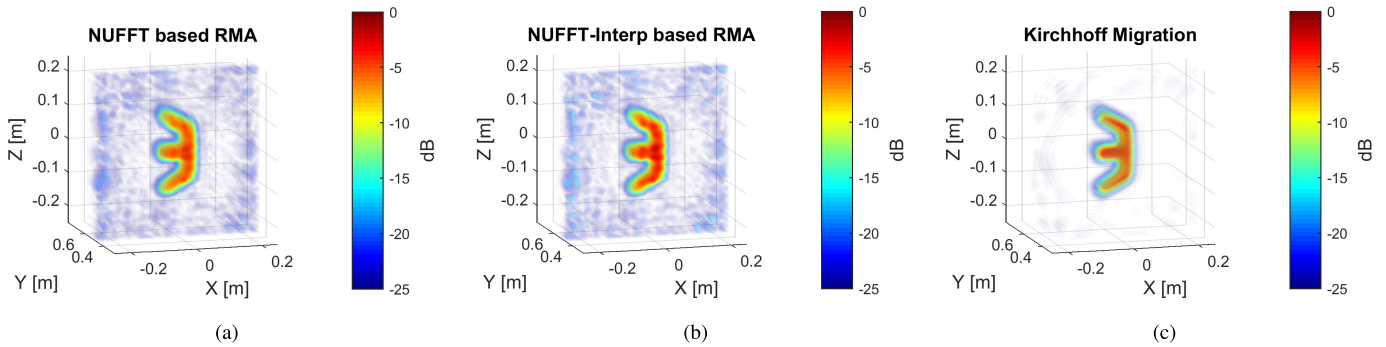
Fig. 4. 3-D images reconstructed with (a) NUFFT-based MIMO RMA, (b) NUFFT-interpolation based MIMO RMA, and (c) Kirchhoff migration, respectively. The operating bandwidth is from 9 to 12 GHz.

TABLE I
PARAMETERS USED FOR THE NUMERICAL SIMULATION WITH THE IRREGULAR MIMO ARRAYS

Parameter		Value
Dimensions of arrays		0.5 m×0.5 m
MIMO array I	No. of transmitter	70
	No. of receiver	75
MIMO array II	No. of transmitter	40
	No. of receiver	50
Operating bandwidths		5−15 GHz & 9−12 GHz
Frequency step		100 MHz
Distance to the target		0.5m

weighted by the areas of the related surrounding Voronoi cells. Fig. 2(b) and (c) shows the Voronoi diagrams of the transmit and receive arrays, respectively. Note that the Voronoi cells associated with the outermost nodes (i.e., antennas) may be unbounded. That is to say, the area of the corresponding Voronoi cell could be infinite. Generally, to tackle this problem, an area that is comparable to those associated with the inner nodes can be assigned to these unbounded Voronoi cells. Although different values can be chosen in implementation, they only cause slight variation of the side-/grating-lobe levels of focused images according to our experience. In this article, we assign the maximum of the areas of the Voronoi cells attached to the inner nodes to the unbounded cells. In practice, some other sophisticated schemes can be used to allocate a more proper area to those unbounded cells based on, for instance, the constraints of dimensions of practical arrays. Nevertheless, this problem is beyond the scope of this article and will be studied in the future. After the weight operation, the 2-D NUFFTs for signal spectrum reconstruction and the 5-D to 3-D data mapping are performed to get focused images. Here, we perform the 5-D to 3-D data mapping by using both 1-D NUFFT-based method and interpolation. The reconstructed 3-D images are shown in Fig. 4(a) and (b). For comparison, the synthetic data are transformed into the time domain by the IFFT. Then, the obtained time-domain data are focused with the modified Kirchhoff migration for MIMO array imaging and the formed image is shown in Fig. 4(c). Fig. 4 shows that all three imaging algorithms produced focused images. However, the image obtained with NUFFT-Interp-based MIMO-RMA

has slightly larger artifacts surrounding the "E"-shaped object than those focused by the modified Kirchhoff migration and NUFFT-based MIMO-RMA, which may result from the error of linear interpolation for the 5-D to 3-D data mapping. On the other hand, both NUFFT- and NUFFT-Interp-based MIMO-RMA are much more computationally efficient than the modified Kirchhoff migration in this case. Specifically, in this imaging example, to reconstruct a 3-D image in a volume $[−0.25, 0.25]$ m $× [0, 0.75]$ m $× [−0.25, 0.25]$ m with sampling intervals of 0.5, 1, and 0.5 cm along the x-, y- and z-axes, NUFFT-based MIMO-RMA, NUFFT-Interp-based MIMO-RMA and the modified Kirchhoff migration took about 36, 104, and 518 s, respectively. All three algorithms are implemented with MATLAB code and run on a computer with Intel i5-3475 central processing unit (CPU) at 3.2 GHz and 8-GB random access memory (RAM). For both NUFFT- and NUFFT-Interp-based MIMO-RMA, parallel computing by using all four cores of the CPU was used to accelerate the signal spectrum reconstruction with two 2-D NUFFTs over different frequencies, which is also applied for the following imaging examples without explicit indication. One can see that in this case NUFFT-based MIMO-RMA is more than 14 times faster and NUFFT-Interp-based MIMO-RMA is five times faster compared to the modified Kirchhoff migration.

To investigate the influence of the signal bandwidth on the imaging performance and efficiency of the proposed method, we also took a simulation with the signal bandwidth from 5 to 15 GHz by using the same array in Fig. 2(a). The same imaging operations as in the previous simulation are taken with the three imaging methods. The imaging results are presented in Fig. 5. By comparing Fig. 4 with Fig. 5, one can see that with the increase of the signal bandwidth the image qualities obtained with all the three methods are improved. Moreover, with a wider signal bandwidth, the images obtained with NUFFT- and NUFFT-Interp-based MIMO-RMA [Fig. 5(a) and (b)] are more comparable to that focused with the Kirchhoff migration [Fig. 4(c)] in contrast to their counterparts in Fig. 4. In terms of the computational efficiency, the NUFFT-based MIMO-RMA, NUFFT-Interp-based MIMO-RMA, and KMA consumed about 53, 123, and 520 s, respectively. Compared with the previous simulation, one can see that the efficiency of the KMA is more or less the same in both bandwidth situations. However, the computational times used by NUFFT-band NUFFT-Interp-based
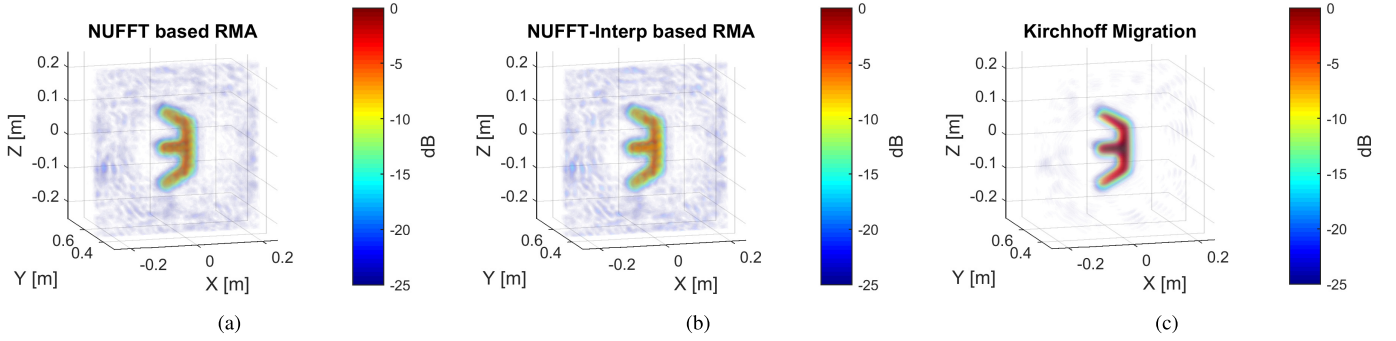
Fig. 5. 3-D images reconstructed with (a) NUFFT-based MIMO RMA, (b) NUFFT-interpolation-based MIMO RMA, and (c) Kirchhoff migration, respectively. The operating bandwidth is from 5 to 15 GHz.
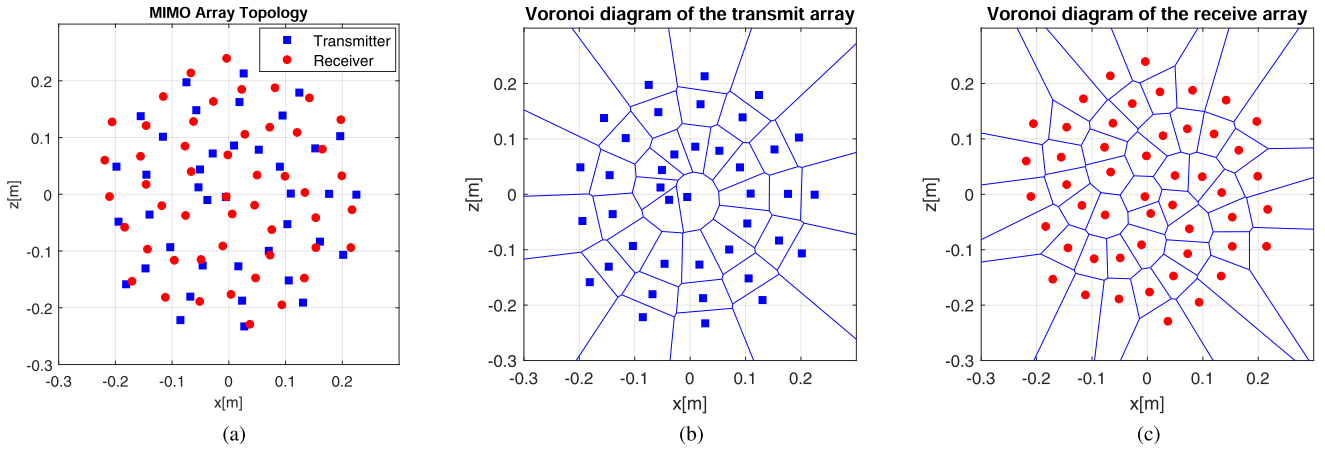

Fig. 6. MIMO array used for numerical simulation. (a) Shows the MIMO array topology formed by 40 transmit and 50 receive antennas. (b) and (c) Display the Voronoi diagrams related to the transmitting and receiving antenna arrays, respectively.

MIMO-RMAs are significantly increased. This is because the KMA performs the image formation in the time–spatial domain, and the computational time is mainly affected by the dimensions of the imaging volume and the number of spatial measurements (i.e., the numbers of transmit and receive antennas). By contrast, the NUFFT- and NUFFT-Interp-based MIMO-RMAs take the focusing operations in the f-k domain; thus, their computational loads go up with the increase of the frequency samples. So, for a fixed frequency sampling step, the NUFFT- and NUFFT-Interp-based MIMO-RMAs take longer time for image reconstruction with a wider signal bandwidth.

Next, 3-D imaging simulations are carried out by using a relatively sparse MIMO array with both signal bandwidths used before, i.e., 9–12 GHz and 5–15 GHz. The sparse MIMO array consists of 40 transmit and 50 receive antennas (MIMO array II in Table I), which are placed along two spiral curves given by

$$
\begin{cases}
x_n = \dfrac{2R\sqrt{(n \cdot N_p + 1)/\pi}}{2\sqrt{N_p N_a/\pi} + 1} \cos[2\pi \tau (N_p \cdot n + 1)] \\
z_n = \dfrac{2R\sqrt{(n \cdot N_p + 1)/\pi}}{2\sqrt{N_p N_a/\pi} + 1} \sin[2\pi \tau (N_p \cdot n + 1)]
\end{cases}
$$
$$n = 0, 1, \ldots, N_a - 1 \quad (17)$$

where $\tau = (1 + \sqrt{5})/2$ is the golden ratio, R represents the radius of the aperture, N_a denotes the number of antennas, and N_p is an auxiliary parameter. In the simulation, we choose $R = 0.25$ m. By setting $N_a = 40$, $N_p = 29$ in (17) for the transmit antennas and $N_a = 50$, $N_p = 31$ for receive antennas, respectively, the MIMO array topology used for our simulation can be obtained, as shown in Fig. 6(a). Again, we use the same "E"-shaped PEC object (shown in Fig. 3) as a target and orient it parallel to the antenna array at a distance of 0.5 m. Similarly, Hertz dipoles are used as radiators of the MIMO array. The synthetic EM signals are generated in the frequency domain by utilizing the EM software FEKO with the MoM solver. The frequency samples are taken with intervals of 100 MHz within the operating bandwidths.

Similar to the previous simulation examples, the synthetic EM data are focused by using three imaging algorithms, i.e., NUFFT-based MIMO-RMA, NUFFT-Interp-based MIMO-RMA, and the modified Kirchhoff migration. To compensate the effects of nonuniform spatial sampling, the synthetic EM data are multiplied by the areas of the corresponding Voronoi cells, as shown in Fig. 6(b) and (c), associated with each sample during the focusing operations of all the three algorithms. For the convenience of comparison, the images are formed over the same grid as the previous simulations. The obtained images with the two operating bandwidths are
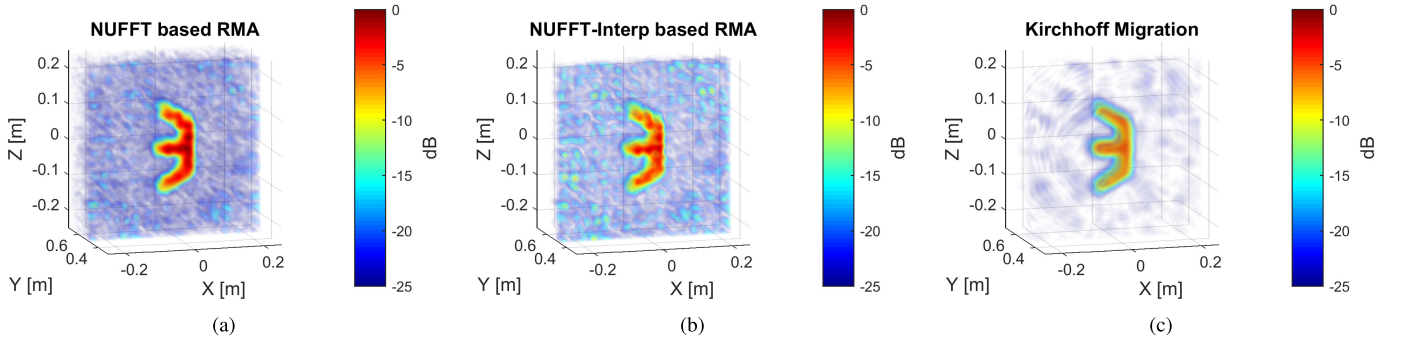
Fig. 7. 3-D images obtained with (a) NUFFT-based MIMO RMA, (b) NUFFT-interp based MIMO RMA, and (c) Kirchhoff migration, respectively. The operating bandwidth is from 9 to 12 GHz.
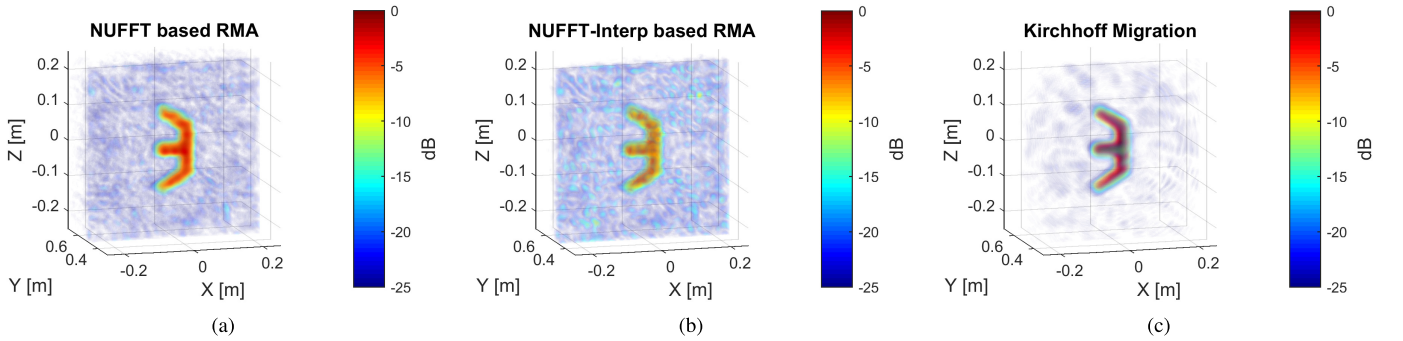

Fig. 8. 3-D images reconstructed with (a) NUFFT-based MIMO RMA, (b) NUFFT-interp based MIMO RMA, and (c) Kirchhoff migration, respectively. The operation bandwidth is from 5 to 15 GHz.

presented in Figs. 7 and 8, respectively. From Figs. 7 and 8, one can see that the "E"-shape of the object is neatly reconstructed in all the images. Comparing the corresponding images in Figs. 7 and 8, it can be seen again that the increase of the signal bandwidth improves the imaging qualities obtained with all the three imaging method. Moreover, the comparisons of the images in Figs. 4 and 7 reveal that with the increase of the sparsity of MIMO arrays the artifacts in the focused images increase. The same phenomenon can be seen from the images in Figs. 5 and 8. According to Fig. 8(a) and (c), the qualities of images obtained with NUFFT-based MIMO-RMA and the KMA are comparable. However, in contrast to Fig. 8(a) and (c), the image in Fig. 8(b) has relatively larger artifacts around the target object, which could be caused by the error of the interpolation for the 5-D to 3-D data mapping in the wavenumber domain. For the imaging process with a bandwidth of 9–12 GHz, the NUFFT-based MIMO-RMA and NUFFT-Interp-based MIMO-RMA took 36 and 103 s while the modified Kirchhoff migration consumed 172 s. Meanwhile, for the signal bandwidth from 5–15 GHz, the computational times of these three imaging methods are about 53, 122, and 173 s, respectively. Comparing with the two previous simulations, the computational efficiency of the modified KMA is significantly improved in a relatively sparse array case due to its low spatial sampling density. By contrast, for the same bandwidth, the NUFFT- and NUFFT-Interp-based MIMO-RMA consume almost constant time regardless of the different sparsity of the MIMO arrays.

To quantitatively compare the focusing performance of the three imaging algorithms, we introduce a power spreading ratio that is defined as the power spreading outside the object normalized to the power within the object volume. It is given by

$$\alpha = P_o / P_i \tag{18}$$

where P_o denotes the power spreading outside the object in the focused image and P_i is the power within the object volume. Table II shows the power spreading ratios of the images (i.e., Figs. 4, 5, 7, and 8) for the four simulations above with different imaging algorithms. It can be seen that the power spreading ratios of the images obtained with both NUFFT- and NUFFT-Interp-based RMAs are much closer to that reconstructed with Kirchhoff migration in the first two simulations where a dense spatial sampling was used. This can be visually confirmed by Figs. 4 and 5 where the power intensities within the "E"-shaped object in Figs. 4 and 5 exhibit sharper contrasts relative to the surrounding area compared to their counterparts in Figs. 7 and 8. As a relatively narrow frequency spectrum synthesizes a long pulse with an oscillating tail in the time domain, the signals are, when focused by Kirchhoff migration, partly integrated in some area outside the object. This results in a relatively larger power spreading ratio than that at a wider signal bandwidth (see the values of 9–12 GHz vs. those of 5–15 GHz in Table II). Moreover, for the sparse array in the last two simulations, the spatial undersampling relative to the high frequencies within the operational bandwidth causes aliasing

TABLE II

POWER SPREADING RATIOS OF THE IMAGES RECONSTRUCTED WITH THE NUFFT-BASED RMA, NUFFT-INTERP-BASED RMA, AND KIRCHHOFF MIGRATION AND THEIR CORRESPONDING COMPUTATIONAL TIME

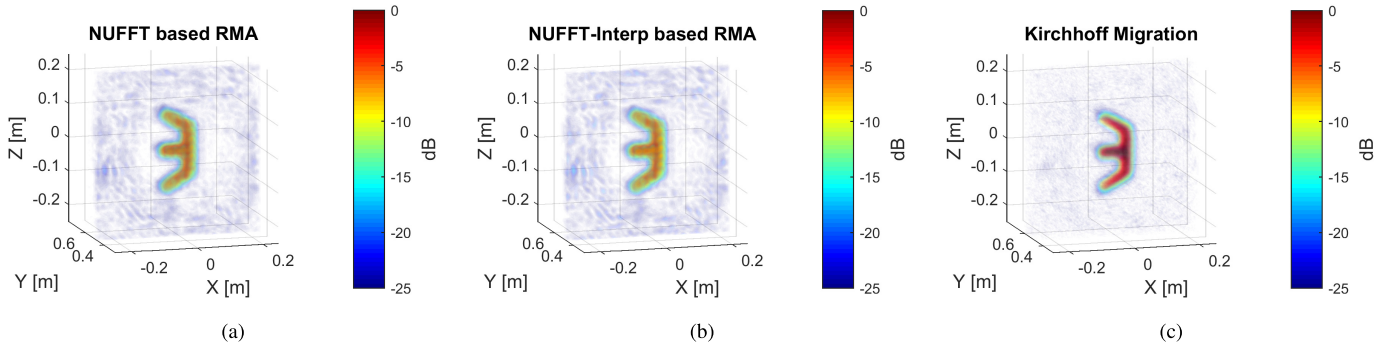|		Array I		Array II	
		9-12GHz	5-15GHz	9-12GHz	5-15GHz
NUFFT-based RMA	α	0.3641	0.2891	0.6369	0.5630
	Time[s]	36	53	36	53
NUFFT-Interp-based RMA	α	0.3664	0.2943	0.6990	0.5772
	Time[s]	104	123	103	122
Kirchhoff migration	α	0.2539	0.1853	0.2782	0.2343
	Time[s]	518	520	172	173

Fig. 9.   3-D images reconstructed with (a) NUFFT-based MIMO RMA, (b) NUFFT-interp based MIMO RMA, and (c) Kirchhoff migration, respectively. The same MIMO array and signal bandwidth as that for Fig. 5 are used, but the signal-to-noise ratio is 5 dB.

after performing the FFT operations. Consequently, the aliased signal spectrum cannot be correctly coherently integrated in the object volume, which forms strong spreading artifacts in the image and deteriorates the power spreading ratio (see the fifth and sixth columns in Table II). At the same time, the ultra-wideband (UWB) frequency spectrum forms a very short pulse in the time domain which limits the interference region in space when the signals measured at different spatial positions are focused with Kirchhoff migration. As a result, Kirchhoff migration produces a sharp image with high power concentration in the object volume.

Furthermore, one additional simulation was performed to investigate the impact of SNR on the imaging performance of the proposed imaging algorithm. The array topology in Fig. 2(a) with the operating bandwidth from 5 to 15 GHz was used. The synthetic EM data in the frequency domain were first transformed into time-domain via the FFT algorithm. Then, Gaussian noises were added to the synthetic signals with an SNR of 5 dB. After that, the obtained signals were processed with the three imaging algorithms. The focused images are shown in Fig. 9. Comparing the corresponding images in Figs. 5 and 9, the noise-contaminated signals result in only small differences in the focused images obtained with the three imaging algorithm. This is because the imaging process drastically improves the SNR of the focused images compared to the input signals. So, one can see that all the three imaging algorithms work well even in a relatively low SNR situation.

V. EXPERIMENTAL RESULTS

This section presents the experimental results of 3-D imaging with an ultrasparse UWB MIMO array. The experimental measurement campaign was performed in the anechoic

chamber in the Delft University of Technology (TU Delft). An ultrasparse MIMO array formed by 16 transmit and 9 receive antennas, as shown in Fig. 10(a), was used for signal acquisition. In the MIMO array, Vivaldi antennas with an operational bandwidth from 3 to 27 GHz were used as transmitters and receivers. All the antennas within the MIMO array were connected to a vector network analyzer (VNA) through a multiport switch [see Fig. 11(b)] which was controlled by a computer. A toy revolver was used as a target and placed in front of the antenna array at a distance of approximately 0.5 m. By sequentially switching on and off each pair of the combinations of the transmit and receive antennas, 144 spatial measurements of the scattered fields from the target were collected. The operating frequency ranged from 5 to 18 GHz with steps of 100 MHz. The background reflections and the time-delays caused by the cables for all the transmit-receive channels were also measured for calibration.

By subtracting the background reflections, the scattered signals from the surrounding environment can be suppressed. The acquired signals were multiplied by a phase correction term to correct time delays caused by the corresponding transmit–receive channel. After these preprocessing steps, the EM signals were focused with the proposed algorithm. To account for the spatial weighting effect, the acquired frequency-domain signals were first multiplied by the areas of their corresponding Voronoi cells over the aperture. The Voronoi diagrams of the transmitters and receivers of the MIMO array are displayed in Fig. 10(b) and (c). The reconstruction of the wavenumber-domain spectra with the 2-D NUFFTs and the 5-D to 3-D data mapping was then performed. Similar to the simulations presented in Section IV, the 5-D to 3-D data mapping was implemented with both the NUFFT-based method and linear interpolation method. The focused images are shown
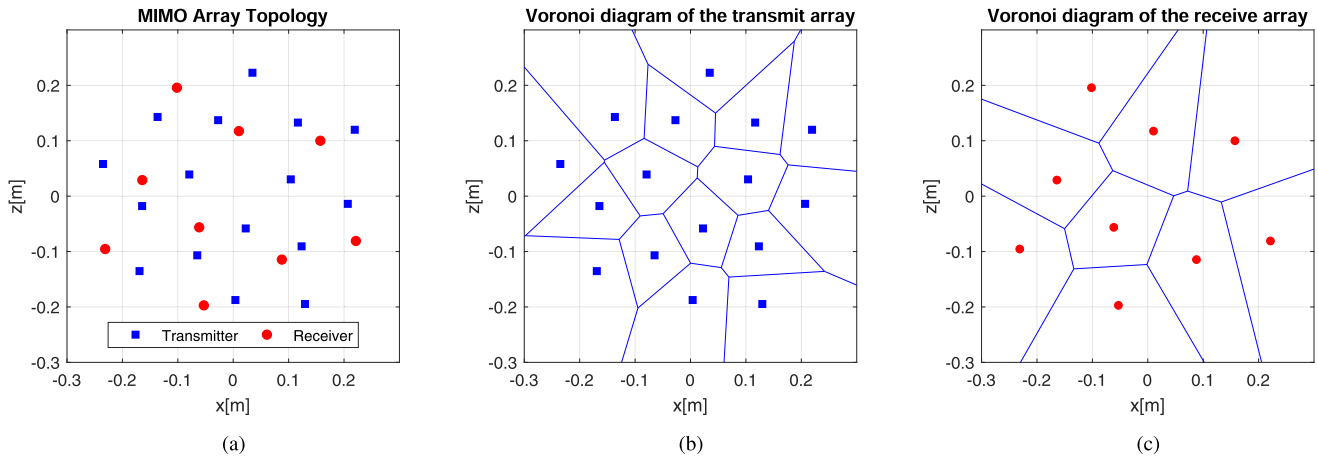
Fig. 10. MIMO array topology used for experimental measurement. (a) MIMO array topology formed by 16 transmit and 9 receive antennas. (b) and (c) Voronoi diagrams related to the transmit and receive antenna arrays, respectively.
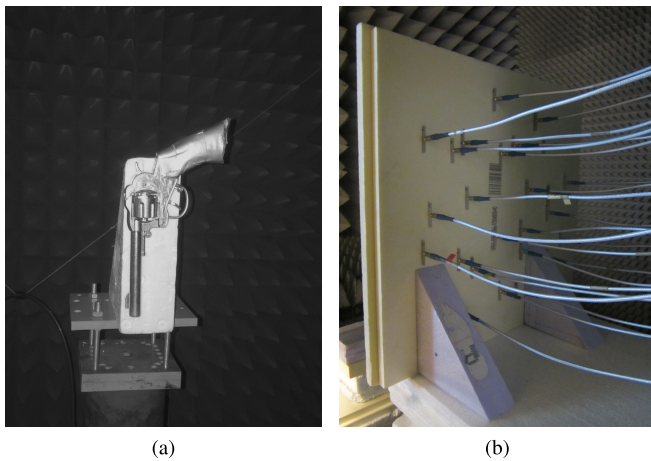

Fig. 11. Experimental setup for MIMO array imaging. (a) Toy revolver target. (b) Setup of the MIMO array.

in Fig. 12(a) and (b), respectively. For comparison, the EM data obtained after preprocessing were also focused with the modified Kirchhoff migration and the reconstructed image is displayed in Fig. 12(c).

Fig. 12 shows that the images of the toy revolver are well reconstructed with all three imaging algorithms. However, much larger artifacts appear in Fig. 12(a) and (b) in contrast to Fig. 12(c). This can be explained as follows. The MIMO array used in the experiment took extremely sparse spatial samples. By applying the 2-D NUFFT, which is also developed by utilizing the FFT algorithm, for spectrum reconstruction, the sparse spatial samples lead to strong aliasing in the wavenumber domain, especially for high operating frequencies. After focusing operations in the f-k domain and wavenumber domain, the aliasing error results in large and widespread artifacts in the focused image. By contrast, the modified Kirchhoff migration directly reconstructs the image in the time–space domain. Thanks to the UWB measurements in the frequency domain, a very short pulse can be constructed in the time domain, which together with the ultrasparse MIMO array leads to an extremely confined interference region in space. Hence, the relatively

large artifacts ascribed to constructive interference are only observed in a very small region around the target [see Fig. 12(c)]. Considering the noticeable differences of the artifacts in the three images in Fig. 12 and the complex structure of the toy revolver which makes it difficult to define a precise object volume, here we omit the quantitative comparison of their power spread ratios.

Moreover, to facilitate the comparison of computational efficiency of the three algorithms, the three images were reconstructed over a common volume with dimensions of $[-0.25, 0.25]$ m $\times$ $[0, 0.75]$ m $\times$ $[-0.25, 0.25]$ m with sampling intervals of 0.5 cm along the x-, y- and z-axes. The time spent by the NUFFT-based MIMO-RMA, NUFFT-Interp-based MIMO-RMA, and the modified Kirchhoff migration is 79, 125, and 27 s, respectively. In this case, the modified Kirchhoff migration is the most efficient of the three imaging algorithms and almost three times faster than the NUFFT-based MIMO-RMA. Hence, for the ultrasparse UWB MIMO array imaging, the modified Kirchhoff migration outperforms the NUFFT- and NUFFT-Interp-based MIMO-RMAs in terms of both imaging quality and computational efficiency. Meanwhile, one can see that the NUFFT-based MIMO-RMA is still much more efficient than the NUFFT-Interp-based MIMO-RMA. In addition, it should be mentioned that to reconstruct images of the volume defined above, in principle, a frequency step larger than 100 MHz (i.e., signal downsampled) in the frequency domain can be used to accelerate the NUFFT- and NUFFT-Interp-based MIMO-RMAs. Specifically, when the frequency-domain signals were sampled from 5 to 18 GHz with steps of 200 MHz, it took around 60 and 113 s for NUFFT- and NUFFT-Interp based MIMO-RMAs to reconstruct images, respectively. However, they are still much less efficient than the modified Kirchhoff migration and the qualities of the focused images are degraded. To save space, the imaging results are omitted here.

VI. DISCUSSION

The simulation results presented in the previous sections show that the NUFFT- and NUFFT-Interp-based MIMO-RMAs are much more efficient than the modified Kirchhoff
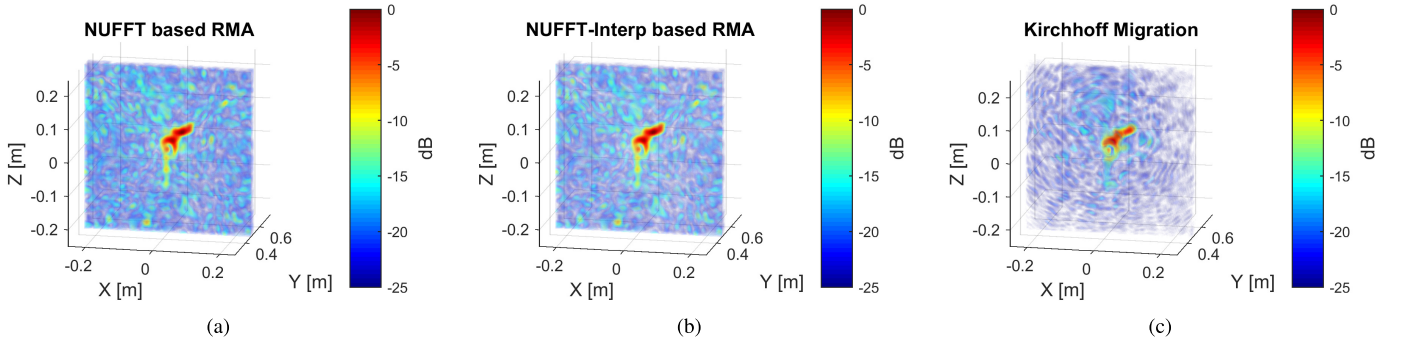
Fig. 12. 3-D images obtained with the experimental measurements. The images are formed by using (a) NUFFT based MIMO RMA, (b) NUFFT-interp based MIMO RMA, and (c) Kirchhoff migration, respectively.

TABLE III

COMPUTATIONAL COMPLEXITY ANALYSIS OF THE NUFFT-BASED MIMO RMA AND NUFFT-INTERP BASED MIMO RMA

Operations	Computational complexity
NUFFTs over the transmit array	$N_f[N_t(3 + 4M_{sp} + 4M_{sp}^2) + N_{kx}^t N_{kz}^t \log(N_{kx}^t N_{kz}^t)]$
NUFFTs over the receive array	$N_f N_{kx}^t N_{kz}^t [N_r(3 + 4M_{sp} + 4M_{sp}^2) + N_{kx}^r N_{kz}^r \log(N_{kx}^r N_{kz}^r)]$
5-D to 3-D mapping by NUFFT†	$N_{kx}^t N_{kz}^t N_{kx}^r N_{kz}^r [N_f(2 + 4M_{sp}) + N_y \log N_y + N_y] - (N_{kx}^t + N_{kx}^r - 1)(N_{kz}^t + N_{kz}^r - 1)N_y$
2-D IFFT†	$(N_{kx}^t + N_{kx}^r - 1)(N_{kz}^t + N_{kz}^r - 1) \log[(N_{kx}^t + N_{kx}^r - 1)(N_{kz}^t + N_{kz}^r - 1)]$
5-D to 3-D mapping by interpolation‡	$(p + 1)N_y N_{kx}^t N_{kz}^t N_{kx}^r N_{kz}^r - (N_{kx}^t + N_{kx}^r - 1)(N_{kz}^t + N_{kz}^r - 1)N_y$
3-D IFFT‡	$(N_{kx}^t + N_{kx}^r - 1)(N_{kz}^t + N_{kz}^r - 1)N_y \log[(N_{kx}^t + N_{kx}^r - 1)(N_{kz}^t + N_{kz}^r - 1)N_y]$

† operations of NUFFT-based MIMO RMA; ‡ operations of NUFFT-Interp based MIMO RMA.

migration but achieve comparable imaging performance for dense MIMO array imaging with narrow-band signals. However, in UWB sparse MIMO array cases, they are inferior in terms of both imaging quality and computational efficiency. These observations about the three imaging algorithms are closely related to their operating domains and processing operations.

To reconstruct high-quality images, the scattered signals acquired by MIMO antenna arrays must be accurately focused. The modified Kirchhoff migration backpropagates the scattered signals in the time–space domain to the time zero to produce focused images. It is applicable to microwave imaging with a generic MIMO array as long as the time-domain scattered signals are precisely acquired. By contrast, the NUFFT- and NUFFT-Interp-based MIMO-RMAs focus the scattered signals in the wavenumber domain. For these two algorithms, the signal spectra in the f-k domain are computed through the 2-D NUFFT, which is devised with the aid of FFT, over the aperture. Thus, to get relatively accurate signal spectra in the f-k domain, the spatial samples acquired by an MIMO antenna array along different directions should be dense enough to fulfill the Nyquist criterion. Otherwise, the employment of the NUFFT on the scattered signals would cause aliasing of the signal spectra in the f-k domain, which leads to smeared artifacts in the focused images. So, NUFFT- and NUFFT-Interp-based MIMO-RMAs are not optimal algorithms for high-quality imaging with UWB ultrasparse arrays. For instance, the ultrasparse UWB MIMO array used for the experimental measurement took very sparse spatial samples

of the scattered fields, which violates the Nyquist criterion for the high operating frequencies. This leads to strong smeared artifacts in the images reconstructed by NUFFT- and NUFFT-Interp-based MIMO-RMAs [see Fig. 12(a) and (b)]. In addition, for sparse arrays the aliasing of the signal spectra computed with the NUFFT algorithm could be alleviated by taking advantage of signal estimation approaches, for instance, the Bayesian estimation method [32]. But it would significantly increase the computational cost of the NUFFT- and NUFFT-Interp-based MIMO-RMAs, which would make them even less appealing for 3-D imaging with sparse arrays as indicated below.

In terms of computational efficiency, the modified Kirchhoff migration is preferred for microwave imaging with ultrasparse UWB MIMO arrays while the NUFFT-based MIMO-RMA is best when relatively dense MIMO arrays are used. Specifically, the computational complexity of the modified Kirchhoff migration is about $16 N_x N_y N_z N_t N_r + N_t N_r N_f \log N_f$, where N_x, N_y, and N_z denote the numbers of grid points of the reconstructed image along the x-, y-, and z-axes, respectively; N_f is the number of frequency samples. The computational cost of the NUFFT- and NUFFT-Interp-based MIMO-RMA are analyzed and presented in Table III. In Table III, as for the modified Kirchhoff migration, N_y is the number of points of the reconstructed image along the y-direction, p is a constant related to the interpolation method used for $k \rightarrow k_y$ mapping, and M_{sp} is the spreading distance of the gridding kernel that controls the accuracy of the NUFFT. For single precision accuracy $M_{sp} = 6$ while $M_{sp} = 12$ for double

precision [21]. N_{kx}^t, N_{kz}^t, N_{kx}^r, and N_{kz}^r are the numbers of grid points along the k_{x_t}, k_{z_t}, k_{x_r}, and k_{z_r} directions after taking the 2-D NUFFTs over the transmit and receive arrays, respectively. Note that frequency-domain signals are assumed for the computational complexity analysis in Table III. For time-domain signals, FFT operations with respect to time are needed before taking NUFFTs over the space, which would slightly increase the computational load.

According to Table III, the NUFFT over the receive array and the 5-D to 3-D data mapping dominant the computational load of the NUFFT- and NUFFT-Interp-based MIMO-RMAs. Fortunately, the NUFFT over the receive array at different frequencies can be computed in parallel, thus improving the computational efficiency. So the computational complexity of the NUFFT- and NUFFT-Interp-based MIMO-RMAs can be approximately estimated by the computational cost of the 5-D to 3-D data mapping. For the NUFFT-based MIMO-RMA, it is around $N_{kx}^t N_{kz}^t N_{kx}^r N_{kz}^r (26N_f + N_y \log N_y + N_y)$ when single precision accuracy is considered. Assuming $N_{kx}^t = N_{kx}^r = N_x/2$ and $N_{kz}^t = N_{kz}^r = N_z/2$, then its computational complexity can be rewritten as $N_x^2 N_z^2 N_y (26N_f/N_y + \log N_y + 1)/16$. As N_f is usually smaller or comparable to N_y, the differences of the computational complexities of the modified Kirchhoff migration and the NUFFT-based MIMO-RMA are roughly determined by the relation between $16N_t N_r$ and $N_x N_z$. Therefore, with dense MIMO arrays, i.e., $16N_t N_r \geq N_x N_z$, NUFFT-based MIMO-RMA is more efficient for 3-D imaging while the modified Kirchhoff migration is even faster in the ultrasparse array cases.
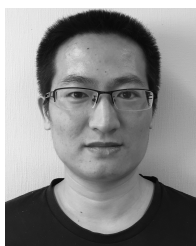
VII. CONCLUSION

In this article, two NUFFT-based MIMO-RMA methods are proposed for efficient 3-D imaging with generic planar MIMO arrays. Based on the two different implementation methods for the 5-D to 3-D data mapping, we distinguish them as NUFFT- and NUFFT-Interp-based MIMO-RMAs, respectively. Through numerical simulations, we have shown that for dense MIMO arrays the proposed algorithm reconstructs high-quality 3-D images with much higher computational efficiency compared to the modified Kirchhoff migration. However, for UWB ultrasparse arrays, the undersampling in space relative to the high frequencies leads to severe aliasing of signal spectra in the wavenumber domain after taking the NUFFTs over the MIMO array aperture, which causes strong artifacts in the focused images. As the sparsity of MIMO arrays increases, the advantage of the high efficiency of NUFFT-based MIMO-RMA gradually diminishes in contrast to the modified Kirchhoff migration, which has been confirmed through computational complexity analysis. By utilizing the 1-D NUFFT to replace the interpolation needed for the data mapping, the NUFFT-based MIMO-RMA is significantly improved compared to the NUFFT-Interp-based method. The computational complexity analysis also provides a guideline to select imaging algorithms: NUFFT-based MIMO-RMA is more efficient for high-quality 3-D imaging with dense MIMO arrays whereas the modified Kirchhoff migration is faster for ultrasparse cases.

REFERENCES

[1] D. Sheen, D. Mcmakin, and T. Hall, "Three-dimensional millimeter-wave imaging for concealed weapon detection," *IEEE Trans. Microw. Theory Techn.*, vol. 49, no. 9, pp. 1581–1592, 2001.

[2] H. M. Jol, *Ground Penetrating Radar Theory and Applications*. Amsterdam, The Netherlands: Elsevier, 2009.

[3] M. Amin, *Through-the-Wall Radar Imaging*. Boca Raton, FL, USA: CRC Press, 2016. Accessed: Dec. 19, 2017. [Online]. Available: https://books.google.nl/books?id=JkzRBQAAQBAJ

[4] Z. Li, J. Wang, J. Wu, and Q. H. Liu, "A fast radial scanned near-field 3-D SAR imaging system and the reconstruction method," *IEEE Trans. Geosci. Remote Sens.*, vol. 53, no. 3, pp. 1355–1363, Mar. 2015.

[5] D. Sheen, D. Mcmakin, and T. Hall, "Near-field three-dimensional radar imaging techniques and applications," *Appl. Opt.*, vol. 49, no. 19, p. E83, Jul. 2010.

[6] J. Wang, P. Aubry, and A. Yarovoy, "A novel approach to full-polarimetric short-range imaging with copolarized data," *IEEE Trans. Antennas Propag.*, vol. 64, no. 11, pp. 4733–4744, Nov. 2016.

[7] J. Wang, P. Aubry, and A. Yarovoy, "A novel rotated antenna array topology for near-field 3-D fully polarimetric imaging," *IEEE Trans. Antennas Propag.*, vol. 66, no. 3, pp. 1584–1589, Mar. 2018.

[8] X. Zhuge and A. G. Yarovoy, "A sparse aperture MIMO-SAR-based UWB imaging system for concealed weapon detection," *IEEE Trans. Geosci. Remote Sens.*, vol. 49, no. 1, pp. 509–518, Jan. 2011.

[9] F. Gumbmann and L.-P. Schmidt, "Millimeter-wave imaging with optimized sparse periodic array for short-range applications," *IEEE Trans. Geosci. Remote Sens.*, vol. 49, no. 10, pp. 3629–3638, Oct. 2011.

[10] J. Gao, B. Deng, Y. Qin, H. Wang, and X. Li, "An efficient algorithm for MIMO cylindrical millimeter-wave holographic 3-D imaging," *IEEE Trans. Microw. Theory Techn.*, vol. 66, no. 11, pp. 5065–5074, Nov. 2018.

[11] J. Gao, Y. Qin, B. Deng, H. Wang, and X. Li, "Novel efficient 3D short-range imaging algorithms for a scanning 1D-MIMO array," *IEEE Trans. Image Process.*, vol. 27, no. 7, pp. 3631–3643, Jul. 2018.

[12] W. F. Moulder *et al.*, "Development of a high-throughput microwave imaging system for concealed weapons detection," in *Proc. IEEE Int. Symp. Phased Array Syst. Technol. (PAST)*, Oct. 2016, pp. 1–6.

[13] J. Laviada, A. Arboleya-Arboleya, and F. Las-Heras, "Multistatic millimeter-wave imaging by multiview portable camera," *IEEE Access*, vol. 5, pp. 19259–19268, 2017.

[14] X. Zhuge and A. G. Yarovoy, "Study on two-dimensional sparse MIMO UWB arrays for high resolution near-field imaging," *IEEE Trans. Antennas Propag.*, vol. 60, no. 9, pp. 4173–4182, Sep. 2012.

[15] S. S. Ahmed, A. Genghammer, A. Schiessl, and L. P. Schmidt, "Fully electronic E-band personnel imager of 2m² aperture based on a multistatic architecture," *IEEE Trans. Microw. Theory Techn.*, vol. 61, no. 1, pp. 651–657, Jan. 2013.

[16] S. S. Ahmed, A. Schiessl, and L.-P. Schmidt, "A novel fully electronic active real-time imager based on a planar multistatic sparse array," *IEEE Trans. Microw. Theory Techn.*, vol. 59, no. 12, pp. 3567–3576, Dec. 2011.

[17] X. Zhuge and A. G. Yarovoy, "Three-dimensional near-field MIMO array imaging using range migration techniques," *IEEE Trans. Image Process.*, vol. 21, no. 6, pp. 3026–3033, Jun. 2012.

[18] T. Fromenteze, O. Yurduseven, F. Berland, C. Decroze, D. R. Smith, and A. G. Yarovoy, "A transverse spectrum deconvolution technique for MIMO short-range Fourier imaging," *IEEE Trans. Geosci. Remote Sens.*, vol. 57, no. 9, pp. 6311–6324, Sep. 2019.

[19] L.-G. Wang, L. Li, J. Ding, and T. J. Cui, "A fast patches-based imaging algorithm for 3-D multistatic imaging," *IEEE Geosci. Remote Sens. Lett.*, vol. 14, no. 6, pp. 941–945, Jun. 2017.

[20] A. Dutt and V. Rokhlin, "Fast Fourier transforms for nonequispaced data," *SIAM J. Sci. Comput.*, vol. 14, no. 6, pp. 1368–1393, 1993.

[21] L. Greengard and J.-Y. Lee, "Accelerating the nonuniform fast Fourier transform," *SIAM Rev.*, vol. 46, no. 3, pp. 443–454, Jan. 2004.

[22] B. Subiza, E. Gimeno-Nieves, J. Lopez-Sanchez, and J. Fortuny-Guasch, "An approach to SAR imaging by means of non-uniform FFTs," in *Proc. IEEE Int. Geosci. Remote Sens. Symp. (IGARSS)*, vol. 6, Jun. 2004, pp. 4089–4091.

[23] J. Song, Q. Huo Liu, P. Torrione, and L. Collins, "Two-dimensional and three-dimensional NUFFT migration method for landmine detection using ground-penetrating Radar," *IEEE Trans. Geosci. Remote Sens.*, vol. 44, no. 6, pp. 1462–1469, Jun. 2006.

[24] J. Wang, H. Cetinkaya, and A. Yarovoy, "NUFFT based frequency-wavenumber domain focusing under MIMO array configurations," in *Proc. IEEE Radar Conf.*, May 2014, pp. 1–4.

[25] Y. Kan, Y. Zhu, L. Tang, Q. Fu, and H. Pei, "FGG-NUFFT-based method for near-field 3-D imaging using millimeter waves," *Sensors*, vol. 16, no. 9, p. 1525, Sep. 2016.

[26] J.-H. Tian, J.-P. Sun, S.-T. Lu, Y.-P. Wang, and W. Hong, "NUFFT-based fast reconstruction for sparse microwave imaging," *J. Electromagn. Appl.*, vol. 27, no. 4, pp. 485–495, Mar. 2013.

[27] M. C. Viganó, G. Toso, G. Caille, C. Mangenot, and I. E. Lager, "Sunflower array antenna with adjustable density taper," *Int. J. Antennas Propag.*, vol. 2009, pp. 1–10, Jan. 2009.

[28] W. Malik, H. Khan, D. Edwards, and C. Stevens, "A gridding algorithm for efficient density compensation of arbitrarily sampled Fourier-domain data," in *Proc. IEEE/Sarnoff Symp. Adv. Wired Wireless Commun.*, Oct. 2006, pp. 125–128.

[29] H. Weyl, "Ausbreitung elektromagnetischer wellen Über einem ebenen leiter," *Ann. Phys.*, vol. 365, no. 21, pp. 481–500, 1919.

[30] T. B. Hansen and A. D. Yaghjian, *Plane-Wave Theory of Time-Domain Fields*. Hoboken, NJ, USA: Wiley, 1999.

[31] J. Lopez-Sahcnez and J. Fortuny-Guasch, "3-D radar imaging using range migration techniques," *IEEE Trans. Antennas Propag.*, vol. 48, no. 5, pp. 728–737, May 2000.

[32] K. Hindriks and A. J. W. Duijndam, "Reconstruction of 3-D seismic signals irregularly sampled along two spatial coordinates," *Geophysics*, vol. 65, no. 1, pp. 253–263, Jan. 2000.

Pascal Aubry received the D.E.S.S. degree in electronics and automatics from the Université Pierre et Marie Curie (Paris 6), Paris, France, in 1993.

He was a Young Graduate Trainee with the European Space Research and Technology Centre (ESTEC), Noordwijk, The Netherlands, in 1996, where he was involved in antenna measurements. Since 1997, he has been with the International Research Centre for Telecommunications and Radar, Delft University of Technology (TUD), Delft, The Netherlands. His research interests include antenna measurement techniques, radar system testing, and signal processing and analysis.

Jianping Wang received the B.Sc. degree from the North China University of Technology, Beijing, China, in 2009, the M.Sc. degree from the Beijing Institute of Technology, Beijing, in 2012, and the Ph.D. degree from the Delft University of Technology, Delft, The Netherlands, in 2018, all in electrical engineering.

From August 2012 to April 2013, he was a Research Associate with the University of New South Wales (UNSW), Sydney, NSW, A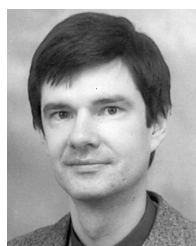ustralia, on frequency modulated continuous wave (FMCW) synthetic aperture radar (SAR) signal processing for formation flying satellites. He is currently a Post-Doctoral Researcher with the Group of Microwave Sensing, Signals and Systems (MS3), Delft University of Technology. His research interests include microwave imaging, signal processing, and antenna array design.

Dr. Wang was a TPC member of IET International Radar Conference, Nanjing, China, in 2018. He was a finalist of the Best Student Paper Awards in International Workshop on Advanced Ground Penetrating Radar (IWAGPR), Edinburgh, U.K., in 2017 and the International Conference on Radar, Brisbane, Australia, in 2018. He has served as a Reviewer for the IEEE TRANSACTIONS ON GEOSCIENCE AND REMOTE SENSING (TGRS), the IEEE GEOSCIENCE AND REMOTE SENSING LETTER (GRSL), the IEEE SENSORS JOURNAL, the IEEE TRANSACTIONS ON IMAGE PROCESSING (TIP), and the *Journal of Applied Geophysics*.

Alexander Yarovoy (Fellow, IEEE) received the diploma degree (Hons.) in radiophysics and electronics, and the Candidate Phys. and Math. Sci. and Doctor Phys. and Math. Sci. degrees in radiophysics from Kharkov State University, Kharkov, Ukraine, in 1984, 1987, and 1994, respectively.

In 1987, he joined the Department of Radiophysics, Kharkov State University as a Researcher, where he became a Professor in 1997. From September 1994 to 1996, he was a Visiting Researcher with the Technical University of Ilmenau, Ilmenau, Germany. Since 1999, he has been with the Delft University of Technology, Delft, The Netherlands. Since 2009, he has been the Chair of Microwave Sensing, Signals and Systems. He has authored or coauthored more than 250 scientific or technical articles and 14 book chapters. He holds four patents. His main research interests are in ultra-wideband (UWB) microwave technology and its applications (particularly radars) and applied electromagnetics (particularly UWB antennas).

Prof. Yarovoy was a recipient of the European Microwave Week Radar Award for the paper that best advances the state of the art in radar technology in 2001 (together with L. P. Ligthart and P. van Genderen) and in 2012 (together with T. Savelyev). In 2010, together with D. Caratelli, he got the Best Paper Award of the Applied Computational Electromagnetic Society (ACES). He served as the Chair and TPC Chair of the 5th European Radar Conference (EuRAD'08), Amsterdam, The Netherlands, and the Secretary of the 1st European Radar Conference (EuRAD04), Amsterdam. He also served as the Co-Chair and TPC Chair of the Xth International Conference on Ground Penetrating Radar (GPR 2004), Delft, The Netherlands. Since 2008, he has been serving as the Director of the European Microwave Association. He served as a Guest Editor of five special issues of the IEEE Transactions and other journals. Since 2011, he has been an Associated Editor of the *International Journal of Microwave and Wireless Technologies*.